Journal of Materials Chemistry A

PAPER

View Article Online
View Journal | View Issue

Cite this: J. Mater. Chem. A, 2015, 3, 23895

Porous ternary $TiO_2/MnTiO_3$@C hybrid microspheres as anode materials with enhanced electrochemical performances†

Shimei Guo,[ac] Jiurong Liu,*[a] Song Qiu,[a] Wei Liu,*[b] Yiran Wang,[d] Nannan Wu,[a] Jiang Guo[d] and Zhanhu Guo*[d]

Received 16th August 2015
Accepted 22nd October 2015

DOI: 10.1039/c5ta06437f

www.rsc.org/MaterialsA

Porous TiO_2/Mn_3O_4 nanocomposite microspheres have been successfully fabricated through impregnating Mn^{2+} ions into the lab-made porous TiO_2, followed by an annealing process. The carbon-coated TiO_2 and $MnTiO_3$ ($TiO_2/MnTiO_3$@C) ternary hybrid composites with a specific surface area of 40.0 $m^2\ g^{-1}$ were obtained by carbonizing the pyrrole coated porous TiO_2/Mn_3O_4 microspheres. The carbon coating with a thickness of 1–2 nm was deposited on the surface and inner wall of pores. Electrochemical tests demonstrated that the as-prepared $TiO_2/MnTiO_3$@C porous electrode materials possessed a reversible capacity of 402.6 mA h g^{-1} after 300 cycles at a current density of 100 mA g^{-1} and the capacities of 259.8, 237.3, 200.4, 150.5 and 103.3 mA h g^{-1} at the current densities of 100, 200, 400, 800, and 1600 mA g^{-1}. The $MnTiO_3/TiO_2$@C porous composites exhibited superior cycling and rate performances, arising from the synergistic effect that was created by little volume variation of the TiO_2 matrix, high capacity of $MnTiO_3$ and good electrical conductivity of the carbon coating during the charge/discharge processes.

1. Introduction

Titanium dioxide (TiO_2), as a band-gap semiconductor material, has attracted considerable attention owing to its unique physicochemical properties and potential applications in environmental and energy areas ranging from photocatalysis, gas sensors, dye-sensitized solar cells and hydrogen generation.[1–4] Especially for lithium ion battery (LIB) applications, TiO_2 has been regarded as one of the most promising candidates to compete with commercial graphite anodes owing to its superior structural stability, long cycle life, high rate performance, low cost and excellent security.[5–7] The current LIB industry has been primarily dominated by graphite as the anode material due to its beneficial layered structure for facile Li^+ insertion/extraction, good electrical conductivity, reasonable cost, and abundant resources. However, in the practical application, the potential for lithium insertion/extraction (0–0.25 V *vs.* Li/Li^+) is close to that of the Li^+/Li redox couple, leading to the possibility of lithium plating during charge and hence generating short out or explosion of LIBs.[8,9] In addition, the formation of a solid electrolyte interphase (SEI) on the graphite surface during initial cycles consumes lots of solvated lithium ions resulting in irreversible capacity loss and limited lifespan.[10–12] In particular, the low theoretical capacity (372 mA h g^{-1}) and poor cycling performance of graphite at higher current density have restricted its large-scale applications in high-power density batteries.[11]

In comparison, TiO_2 undergoes less than 4% volume change, smaller than that of graphite (*ca.* 10%) during lithium ion insertion/extraction processes,[6,12,13] which gives TiO_2 outstanding structural stability, and hence ensuring extended cycle life and fast/high-power charge/discharge processes. Moreover, the TiO_2 anode operates at a relatively high lithium insertion/extraction voltage (1.5–1.8 V *vs.* Li/Li^+),[14,15] which may efficiently restrain the formation of SEI layers and lithium plating on the anode, thereby enabling the enhanced safety of batteries.[16] But, apart from these attractive advantages, as the anode material, TiO_2 usually displays a low theoretical capacity (168–335 mA h g^{-1}), even lower than that of commercial graphite (372 mA h g^{-1}), and poor rate capability due to its low electrical conductivity ($\sim 1 \times 10^{-12}$ to 1×10^{-7} S cm^{-1}) and lithium ion diffusivity ($\sim 1 \times 10^{-15}$ to 1×10^{-9} $cm^2\ s^{-1}$),[12,17,18] which have become the main obstacles for its application in LIBs. Consequently, tremendous endeavor has been devoted to

[a]Key Laboratory for Liquid–Solid Structural Evolution and Processing of Materials, Ministry of Education, School of Materials Science and Engineering, Shandong University, Jinan 250061, China. E-mail: jrliu@sdu.edu.cn; Tel: +86-531-88390236

[b]State Key Laboratory of Crystal Materials, Shandong University, Jinan 250100, China. E-mail: weiliu@sdu.edu.cn

[c]College of Physics and Electronic Engineering, Qujing Normal University, Qujing, Yunnan 655011, China

[d]Integrated Composites Laboratory (ICL), Department of Chemical & Biomolecular Engineering, University of Tennessee, Knoxville, Tennessee 37996, USA. E-mail: zguo10@utk.edu; Tel: +1-865-974-2933

† Electronic supplementary information (ESI) available. See DOI: 10.1039/c5ta06437f

improving the specific capacity and rate capability of TiO_2. So far, all of the strategies can be mainly summarized into two categories. The first strategy is to design various nanostructures, such as nanoparticles,[19] nanowires,[20] nanotubes,[21,22] nanosheets,[22] *etc.*, because the nanostructured electrodes can shorten the pathway for Li-ion diffusion and electron transport as well as provide more contact area with the electrolyte, which may facilitate a higher Li-ion flux across the electrode/electrolyte interface and more Li accommodated at the interface of nanosized electrodes leading to a higher energy density.[6,23–25] Another strategy relies largely on the design of a nanoarchitecture and hybridization of two or multiple active materials in synergy.[23] TiO_2 was made into composites with more conductive materials, including carbonaceous materials (carbon nanotubes, graphene, ordered mesoporous carbon, *etc.*),[26–28] noble metals (Au, Ag, *etc.*),[3,29,30] and RuO_2,[31,32] and/or doped with foreign atoms (W, N, Nb, B, Zn, *etc.*),[33–37] or even served as the robust scaffolds for another active material to construct hybrid electrode materials, such as TiO_2@Fe_2O_3,[23] TiO_2/Co_3O_4,[12] TiO_2–MnO_2/MnO_2,[38] and TiO_2/SnO_2.[39,40] Obviously, amongst the alternative active materials to fabricate TiO_2-based hybrid electrodes, transition metal oxides are the commonly used materials due to their high theoretical capacity, low cost and complementary features with TiO_2. In contrast, transition metal titanates, such as manganese titanate ($MnTiO_3$), ferrous titanate ($FeTiO_3$), and cobalt titanate ($CoTiO_3$), are still an unheeded domain for constructing TiO_2-based hybrid electrodes. According to a few research studies reported in recent years, transition metal titanates also exhibited excellent performance in lithium ion storage compared with their counterparts of transition metal oxides.[41–43] For example, $FeTiO_3$ nanosheets as the anode for LIBs displayed a stable discharge capacity of *ca.* 430 mA h g^{-1} up to 90 cycles at a current density of 100 mA g^{-1}.[42] CoO–$CoTiO_3$ hybrid nanotube arrays not only demonstrated a high capacity (*ca.* 600 mA h g^{-1} after 250 cycles) but also displayed a much better cycling performance (no capacity fading within 250 cycles) than CoO nanowire arrays.[43] Thus, hybridizing transition metal titanates with TiO_2 is considered to be a promising way to enhance the electrochemical performances of TiO_2-based anodes for LIBs. However, to the best of our knowledge, no investigation has been presented on utilizing transition metal titanate and TiO_2 hybrid materials as LIB anodes so far.

In this work, carbon coated TiO_2 and $MnTiO_3$ ($TiO_2/MnTiO_3$@C) ternary hybrid composites were prepared by impregnating Mn^{2+} solution into porous TiO_2 microspheres, followed by calcining at 500 °C for 1 hour and then carbonizing the coated pyrrole. The electrochemical measurements demonstrate that the as-prepared $TiO_2/MnTiO_3$@C porous microspheres exhibit superior cycling and rate performances.

2. Experimental section

2.1 Materials

Tetrabutyl titanate (TBT, $Ti(OC_4H_9)_4$, 99.0%), *N*,*N*-dimethylformamide (DMF, C_5H_9NO, 99.0%), isopropanol (IPA, C_3H_8O, 99.0%), manganese chloride tetrahydrate ($MnCl_2\cdot4H_2O$, 99.0%) and ammonia ($NH_3\cdot H_2O$, 25%) were purchased from Sinopharm Chemical Reagent Co., Ltd. White polyvinylidene fluoride (PVDF, $(C_2H_2F_2)_n$, MW 500 000–700 000) powder was dissolved in absolute *N*-methyl-2-pyrrolidinone (NMP, C_5H_9NO, 99.0%) solvent in a weight ratio of 9 : 91. All the chemicals were of analytical grade and were used as received without further purification.

2.2 Synthesis of porous TiO_2 microspheres

The porous TiO_2 microspheres were prepared by a solvothermal method reported in previous work.[44] In a typical synthesis, 1.0 mL TBT was added to the mixed organic solvent comprising 10 mL DMF and 30 mL IPA without stirring. Then, the resultant solution was quickly transferred into a 70 mL Teflon-lined stainless steel autoclave, and subsequently sealed and heated at 200 °C for 20 h in an oven. After cooling to room temperature naturally, the resultant white precipitate was centrifuged and washed using ethanol five times, and then dried in an oven at 60 °C for 12 h. The porous TiO_2 microspheres were obtained by annealing the white precursor at 400 °C for 3 h in air.

2.3 Synthesis of carbon coated TiO_2 and $MnTiO_3$ ternary hybrid microspheres

Before the synthesis of $TiO_2/MnTiO_3$@C hybrid microspheres, the TiO_2/Mn_3O_4 composites were first prepared as intermediates. Typically, 7.0 g $MnCl_2\cdot4H_2O$ was dissolved in 10 mL deionized water to form a transparent solution under magnetic stirring. Then, 1.6 g as-prepared porous TiO_2 microspheres were dispersed into the above solution and immersed for 4 hours in a vacuum. After filtering, the obtained sample was immersed in 10 mL ammonia solution for 2 hour. The brown precipitate was centrifuged and washed using deionized water and ethanol several times, and then dried in an oven at 60 °C for 12 h. Subsequently, the TiO_2/Mn_3O_4 intermediate was obtained by calcining the brown precipitate at 500 °C for 1 h in air. The product of $TiO_2/MnTiO_3$@C was synthesized as follows. 1.5 g as-prepared TiO_2/Mn_3O_4 microspheres were mixed with 0.5 mL pyrrole in a stainless steel autoclave, and then the tightly sealed autoclave was heated at 550 °C for 5 h in a furnace. During the reaction, pyrrole was carbonized to an amorphous carbon coating and Mn_3O_4 was transformed into $MnTiO_3$ completely by the reaction with excessive carbon and TiO_2, finally forming the $TiO_2/MnTiO_3$@C hybrid microspheres.

2.4 Characterization

The structure of the resultant products was determined by X-ray powder diffraction (XRD) on a Rigaku D/Max-RC X-ray diffractometer with Ni filtered Cu K_α radiation ($\lambda = 0.1542$ nm, $V = 40$ kV, $I = 50$ mA) in the range of 10–80° at a scanning rate of 4° min^{-1}. The morphology and microstructure of the samples were examined by using a JSM-6700F field emission scanning electron microscope (FE-SEM) at an accelerating voltage of 20 kV and an electric current of 1.0×10^{-10} A, and a JEOL JEM-2100 high resolution transmission electron microscope (HR-TEM) operating at 200 kV. The element contents were examined by using an energy-dispersive X-ray spectroscopy (EDS) detector

attached to the FE-SEM. The N_2 adsorption/desorption isotherms of porous products were measured at 77 K on a Quadrasorb-SI instrument. The specific surface area was calculated with the Brunauer–Emmett–Teller (BET) model and the pore size distribution was determined using the Barrett–Joyner–Halenda (BJH) method. The composition was determined by X-ray photoelectron spectroscopy (XPS) on a Kratos Analytical spectrometer, using Al Kα ($h\nu = 1486.6$ eV) radiation as the excitation source at an anode voltage of 12 kV and an emission current of 10 mA. Thermogravimetric analysis (TGA, TA Instruments SDT Q600) was performed in air from ambient temperature to 800 °C at a heating rate of 5 °C min^{-1} using a SDT thermal-microbalance apparatus.

2.5 Electrochemical measurements

To prepare the working electrode, the active material, carbon black, and polyvinylidene fluoride (PVDF) with a weight ratio of 7 : 2 : 1 were mixed in *N*-methyl-2-pyrrolidinone (NMP) to form a homogenous slurry, which was coated on a copper foil substrate, followed by drying in a vacuum oven at 120 °C for 12 h, and then cut into a wafer with an area of 1.54 cm^2. All types of electrodes were comprised of 2–3 mg active material on the current collector, corresponding to 1.3–2 mg cm^{-2} for the mass loading of the active material. The CR2025-type cells were assembled using Li foil as counter and reference electrodes, Celgard 2300 as the separator, and 1 M LiPF6 (dissolved in ethylene carbonate, dimethyl carbonate, and ethylene methyl carbonate with a volume ratio of 1 : 1 : 1) as the electrolyte. The assembly was performed in a glove-box filled with an argon atmosphere. The performance of the cells was evaluated galvanostatically in the voltage range from 0.02 to 3 V at various current densities on a LAND CT2001A battery test system. Cyclic voltammograms (CVs) were obtained by using a PARSTAT 2273 electrochemistry workstation at a scan rate of 0.3 mV s^{-1} and the potential *vs.* Li/Li^+ ranging from 0.01 to 3 V. Electrochemical impedance spectra were recorded on the same instrument with an AC signal amplitude of 10 mV in the frequency range from 100 kHz to 0.01 Hz. The data were adopted to draw Nyquist plots using the real part Z′ as the *X*-axis, and the imaginary part Z″ as the *Y*-axis.

3. Results and discussion

As shown in Fig. 1a, the XRD pattern confirms that all the identified peaks can be assigned to anatase TiO_2 (JCPDS no. 21-1272)[44,45] without any other phase detected, suggesting the high purity of TiO_2. After impregnating Mn^{2+} ions into porous TiO_2 microspheres followed by calcining at 500 °C for one hour in air, the weak peaks of Mn_3O_4 (JCPDS no. 24-0734) can be observed apart from the characteristic peaks of anatase TiO_2 (Fig. 1b), indicating that the TiO_2/Mn_3O_4 composites have been prepared successfully. In Fig. 1c, the XRD peaks could be assigned to rhombohedral $MnTiO_3$ (JCPDS no. 29-0902) and anatase TiO_2 (JCPDS no. 21-1272), and no other diffraction peak was detected, suggesting that Mn_3O_4 has been transformed into $MnTiO_3$ completely by the reaction with carbon and TiO_2. The formed

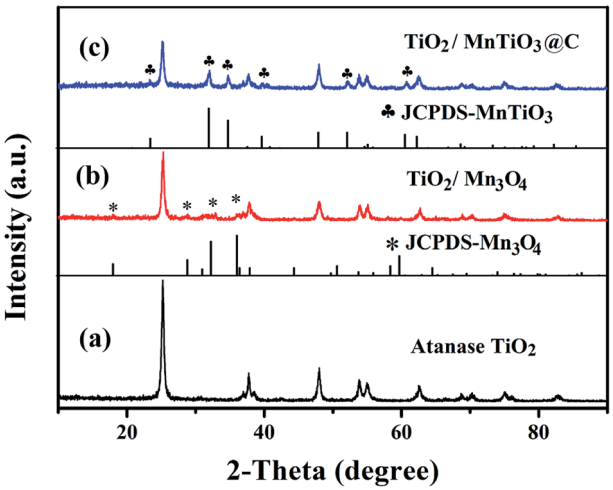

Fig. 1 XRD patterns of (a) anatase TiO_2 precursor, (b) TiO_2/Mn_3O_4 intermediate, and (c) $TiO_2/MnTiO_3$@C.

carbon coating on the $TiO_2/MnTiO_3$ surface was amorphous, consistent with the subsequent HR-TEM observation. In the preparation procedures, the reactions for the formation of the TiO_2/Mn_3O_4 intermediate and $TiO_2/MnTiO_3$@C hybrid composites can be illustrated as follows:

$$Mn^{2+} + 2OH^- \rightarrow Mn(OH)_2\downarrow \quad (1)$$

$$6Mn(OH)_2 + O_2 \rightarrow 2Mn_3O_4 + 6H_2O\uparrow \quad (2)$$

$$Mn_3O_4 + C \rightarrow MnO + CO_2\uparrow \quad (3)$$

$$MnO + TiO_2 \rightarrow MnTiO_3 \quad (4)$$

The low-magnification SEM image indicates that the synthesized TiO_2 is microspheres with a diameter of *ca.* 0.8–1.5 μm and a rough surface (Fig. 2a). Meanwhile, it can be observed that the microspheres built from the two-dimensional nanoflakes have a porous structure. After being impregnated in Mn^{2+} solution and annealed at 500 °C for one hour in air, the microspheres have no obvious variation, but a lot of tiny particles are observed adhering on the nanoflakes or filling into the pores (Fig. 2b). In the HR-TEM image (Fig. 3a), the apparent contrast between the white part and black ligaments on the edge confirms the porous characteristics of microspheres. The black center is attributed to the fact that the size of the spheres is too large to be penetrated completely by the electron beam. From the higher resolution image (Fig. 3b), two sets of lattice fringe spacings of 0.361 and 0.306 nm were observed corresponding to the (101) plane of anatase TiO_2 and the (112) plane of cubic Mn_3O_4, respectively, further demonstrating the simultaneous presence of TiO_2 and Mn_3O_4. Followed by the carbon coating on TiO_2/Mn_3O_4 hybrid microspheres, there is no obvious variation in the morphology and size (Fig. 2c), and the elemental mapping of a selected area on the SEM image (Fig. S1†) reveals a uniform distribution of Ti, Mn, O and C elements. However, from the HR-TEM observation (Fig. 3c), the

obtained $TiO_2/MnTiO_3$@C exhibits a more loose architecture comprised of numerous nanoscale particles and pores compared with TiO_2/Mn_3O_4 microspheres due to the reaction of Mn_3O_4 with carbon and TiO_2. Two sets of lattice fringe spacings of 0.361 and 0.277 nm corresponding to the (101) plane of anatase TiO_2 and the (104) plane of $MnTiO_3$ (Fig. 3d), respectively, were observed. The carbon coating with a thickness of 1–2 nm was found to be deposited on the surface of $MnTiO_3$ and TiO_2 crystallites, confirming the formation of $TiO_2/MnTiO_3$@C porous microspheres.

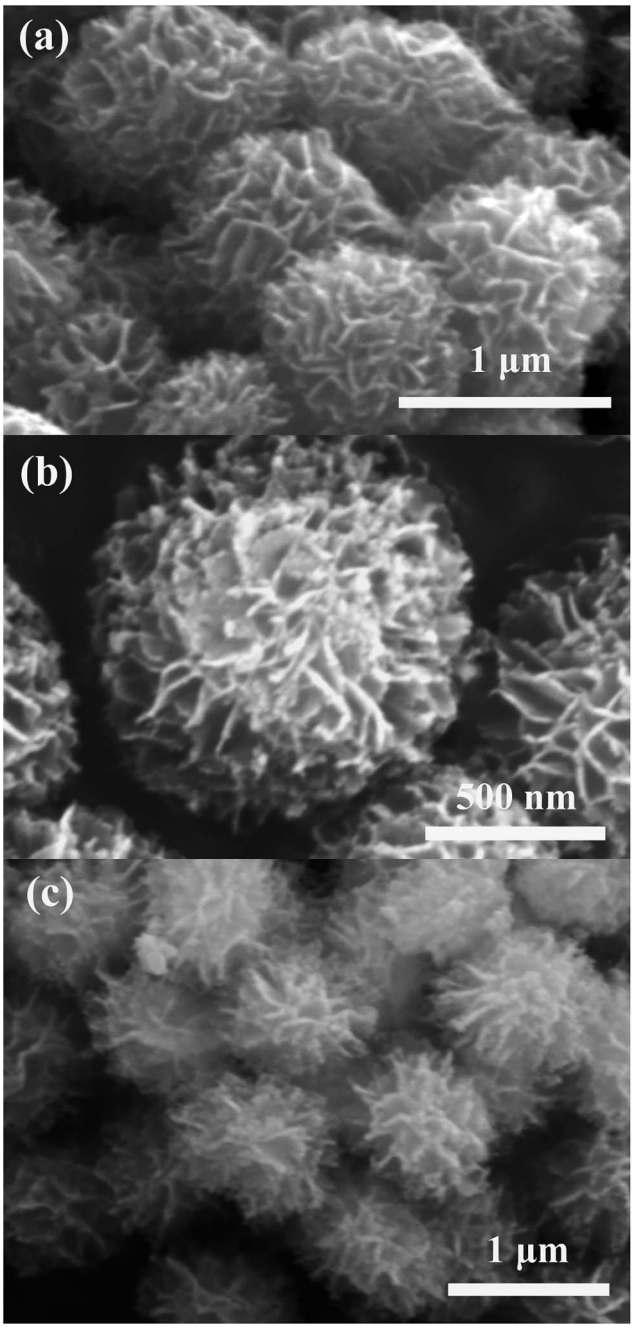

Fig. 2 FE-SEM images of the prepared (a) TiO_2, (b) TiO_2/Mn_3O_4, and (c) $TiO_2/MnTiO_3$@C.

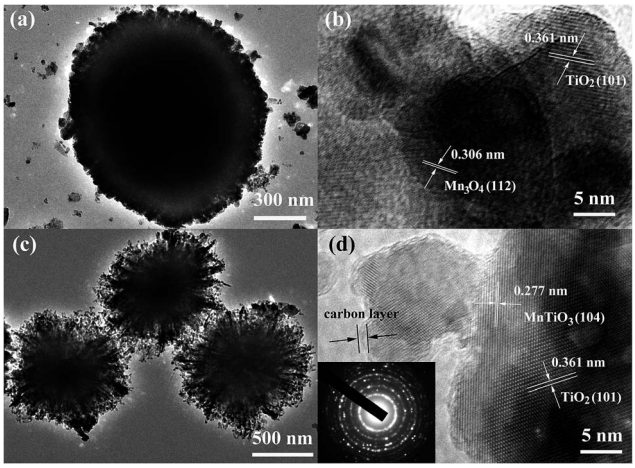

Fig. 3 TEM images of (a) TiO_2/Mn_3O_4 and (c) $TiO_2/MnTiO_3$@C; HR-TEM images of (b) TiO_2/Mn_3O_4 and (d) $TiO_2/MnTiO_3$@C.

A TGA test has been conducted on $TiO_2/MnTiO_3$@C porous microspheres to evaluate the carbon content. As shown in Fig. 4, the weight variation can be separated into three steps. In step (a), from room temperature to 150 °C, the weight loss of *ca.* 0.72% corresponds to the evaporation of water absorbed in the porous microspheres. The dominant weight loss of 4.73%, observed between 150 and 450 °C in step (b), is attributed to the oxidation process of carbon to form volatile species, such as CO and CO_2. After 450 °C, an apparent bullish weight slope suggests that the oxidation reaction from Mn^{2+} to Mn^{3+} begins to occur. Previous studies have confirmed that MnO will be oxidized to Mn_2O_3 after a heat treatment between 500 and 1050 °C in air.[46,47] From the EDS quantitative analysis (Fig. S2†), the atomic ratio of Ti to Mn in the $TiO_2/MnTiO_3$@C sample is 18.78 : 2.34. Combining the EDS with TGA results, the mass fractions of TiO_2, $MnTiO_3$ and C in the hybrid microspheres are calculated to be 75.09, 20.18, and 4.73%, respectively.

As the LIB anode material, the porous structure can facilitate an efficient contact of the internal active materials with the electrolyte, leading to fast transportation of Li^+ ions. Meanwhile, the high specific surface area and porosity are able to

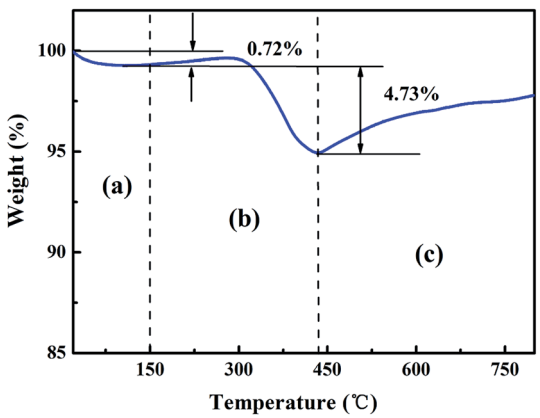

Fig. 4 TGA curve of $TiO_2/MnTiO_3$@C at a heating rate of 5 °C min^{-1} under air flux.

favorably alleviate the volume variation during Li^+ insertion/extraction, resulting in a relatively high reversible capacity and cycling stability.[48,49] Therefore, nitrogen absorption–desorption measurements were performed to investigate the porosity and surface area of the TiO_2/$MnTiO_3$@C porous microspheres and pristine TiO_2 precursor. As shown in Fig. 5, both the nitrogen adsorption/desorption isotherms exhibit a type IV nitrogen adsorption branch with a type-H3 hysteresis loop, indicating the presence of mesopores in the TiO_2 and TiO_2/$MnTiO_3$@C microspheres.[38,45] From the pore size distribution curve (inset of Fig. 5a), the pore size is found to have a nonuniform distribution ranging from several nanometres to 30 nm and the pores with a size of *ca.* 10 nm are dominant. The BET surface area of TiO_2 porous microspheres is 58.4 m^2 g^{-1}, and the pore volume is calculated to be 0.14 cm^3 g^{-1}. While as to the TiO_2/$MnTiO_3$@C sample, the BET surface area and the pore volume are 40.0 m^2 g^{-1} and 0.16 cm^3 g^{-1}, respectively. Moreover, it is observed that the pore size of TiO_2/$MnTiO_3$@C has a wider distribution (inset of Fig. 5b) than that of the TiO_2 sample, and the dominant pore size has been changed to *ca.* 30 nm. These results suggest that the formation of $MnTiO_3$ and the carbon layer in the TiO_2/$MnTiO_3$@C sample does not destroy the porous structure of the TiO_2 matrix, but even increases the pore volume, resulting in a more loose structure due to the consumption of the TiO_2 matrix and the release of CO_2 gas during the carbonization process. The decrease of the BET surface area may be attributed to the formation of $MnTiO_3$ and the deposition of the carbon coating into channels, and hence decreasing the mesopores in the TiO_2 matrix.

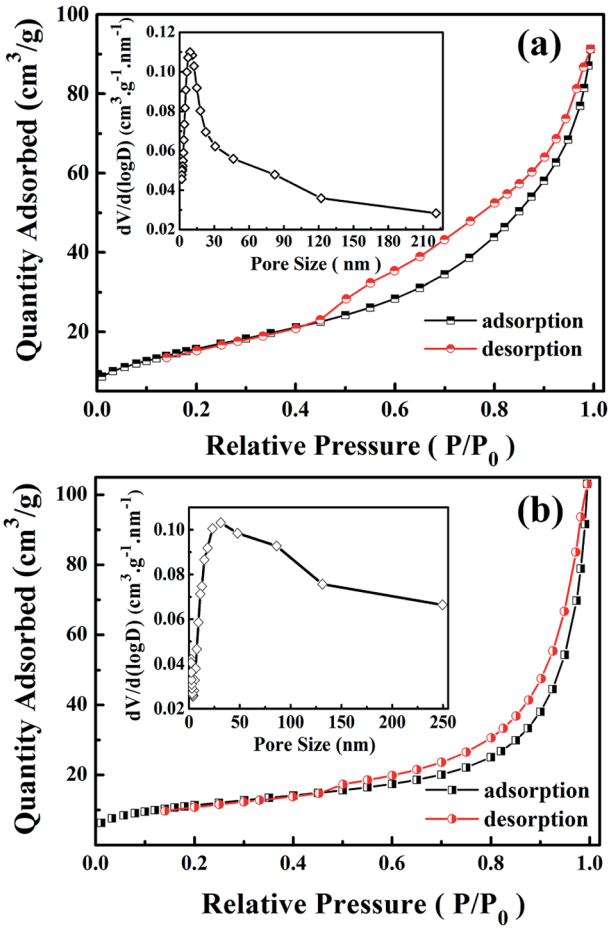

Fig. 5 N_2 adsorption–desorption isotherms of porous (a) anatase TiO_2 and (b) TiO_2/$MnTiO_3$@C microspheres. The insets are pore size distribution curves.

X-ray photoelectron spectroscopy (XPS) analysis was carried out to determine the composition and chemical bonding of TiO_2/$MnTiO_3$@C composites. From the survey scan spectrum (Fig. S2a†), the peaks of Mn 2p, Ti 2p, O 1s, N 1s and C 1s are detected, indicating the existence of Mn, Ti, O, C and N elements. Two peaks at the binding energy of 653.3 and 641.3 eV (Fig. 6a) are assigned to Mn 2p1/2 and Mn 2p3/2, respectively, which are in good agreement with those reported for MnO,[50,51] suggesting the presence of Mn^{2+}. In Fig. 6b, the Ti 2p doublet centered at 458.6 and 464.6 eV stems from Ti 2p3/2 and Ti 2p1/2, respectively.[33] The splitting binding energy between the Ti 2p1/2 and Ti 2p3/2 core levels is 6 eV, indicating a normal state of Ti^{4+} in the product.[33,37] The deconvoluted O 1s peaks at 532.8, 531.5 and 529.8 eV (Fig. 6c) are assigned to O–C, Mn–O–Ti, and Ti–O–Ti, respectively. The C 1s peak is not asymmetrical and could be deconvoluted into four peaks centered at *ca.* 284.6, 285.9, 287.1, and 288.9 eV (Fig. 6d) corresponding to the sp^2C–sp^2C, N–sp^2C, N–sp^3C, and C–O type bonds, respectively.[50,52] For the N 1s spectrum, two deconvoluted peaks around 398.2 and 400.1 eV (Fig. S2b†) are attributed to the formation of pyridinic *N* (398.3 eV) and pyrrolic *N* (400.0 eV) in the carbon coating after the decomposition of pyrrole.[53]

To evaluate the applicability of TiO_2/$MnTiO_3$@C porous microspheres as LIB anode materials, the electrochemical performances were investigated in the voltage window of 0.01–3.0 V. For comparison, pure anatase TiO_2 porous microspheres were also employed as anode materials. Fig. 7a and b show the cyclic voltammetry (CV) curves of TiO_2/$MnTiO_3$@C and pure anatase TiO_2 samples in the initial three cycles, respectively. For pure TiO_2 porous microspheres (Fig. 7a), there are three clear cathodic peaks appearing at *ca.* 0.4, 0.9 and 1.3 V, respectively, in the first discharge process, but the peaks at 0.4 and 0.9 V disappeared from the second discharge process, suggesting the irreversible reduction of the electrolyte and the formation of amorphous Li_2O and solid electrolyte interphase (SEI) layers.[12,17] In the subsequent charge process, only one anodic peak at about 2.3 V is observed. According to the previous studies, the pairs of cathodic/anodic peaks at 1.3 (shifted to 1.6 V from the second cycle) and 2.3 V are the characteristics of the Li^+ insertion/extraction reaction in anatase TiO_2, corresponding to the reversible biphasic transition between tetragonal anatase and orthorhombic Li_xTiO_2 ($TiO_2 + xLi^+ + xe^- \leftrightarrow Li_xTiO_2$).[12,14] There is an observable decrease of cathodic current in the second cycle compared to the first one for the TiO_2 electrode, which agrees with the previous report on the TiO_2 anode and can be attributed to the irreversible lithium insertion/extraction reaction, indicating a large capacity loss during the first two cycles.[14] As to the TiO_2/$MnTiO_3$@C sample (Fig. 7b), two sets of cathodic/anodic peaks at about 0.6/1.3 and 1.6/2.1 V are observed during the first discharge/charge process. Evidently, the couple of 1.6/2.1 V is assigned to anatase TiO_2, consistent

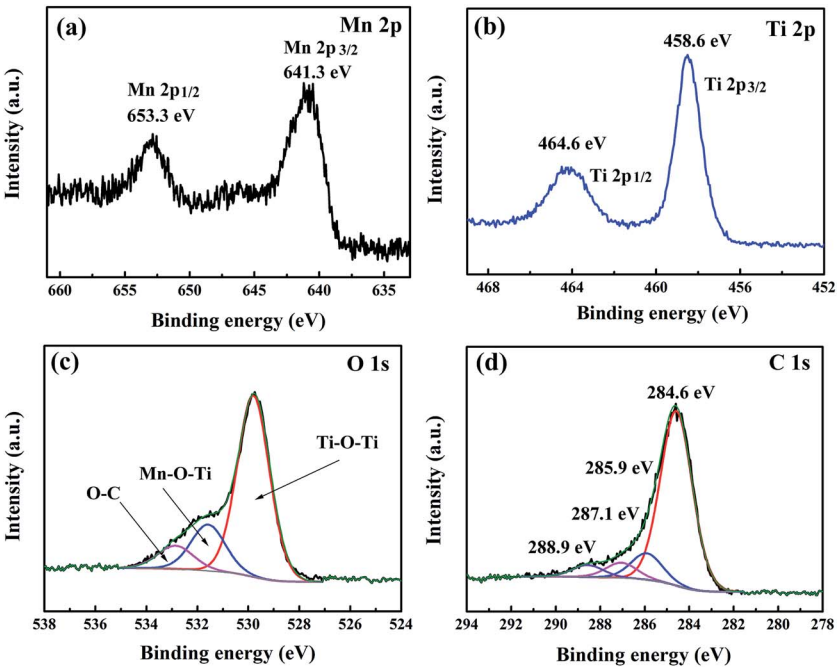

Fig. 6 XPS spectra of (a) Mn 2p, (b) Ti 2p, (c) O 1s and (d) C 1s of TiO_2/$MnTiO_3$@C ternary hybrid microspheres.

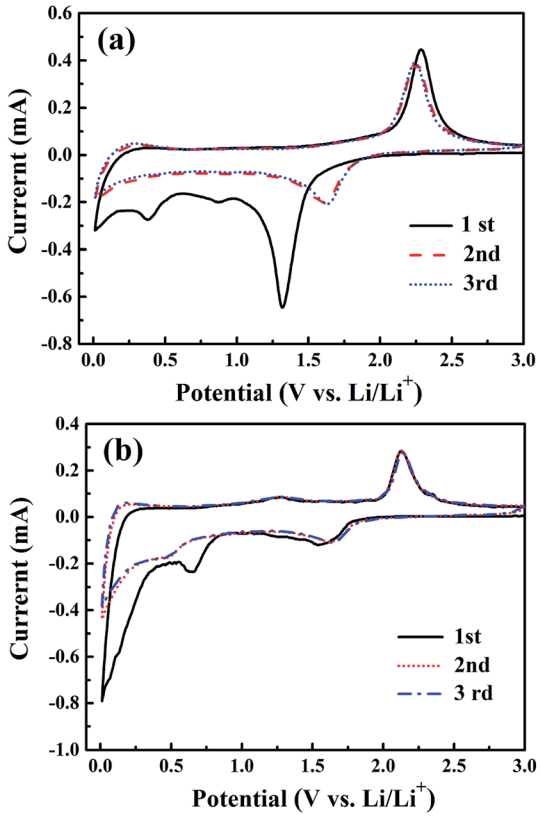

Fig. 7 Cyclic voltammetry (CV) curves of porous (a) pure TiO_2 and (b) TiO_2/$MnTiO_3$@C microspheres at a scanning rate of 0.3 mV s^{-1} in the range of 0.01–3.0 V.

with the above CV results of pure anatase TiO_2 porous microspheres, while the reduction peak around 0.6 V corresponded to the electrochemical reduction reaction of $MnTiO_3$ ($MnTiO_3$ + $3Li^+$ + 3e → Mn + $LiTiO_2$ + Li_2O).[41,42] The observed broad oxidation peak at 1.3 V in the anodic process could be ascribed to the oxidation of Mn^0 to Mn^{2+}.[48,50,51] It is noteworthy that the reduction peak at 0.6 V is weakened and shifted to near 0.5 V after the first cycle, suggesting an irreversible phase transformation due to the formation of Li_2O and metallic manganese. After the second cycle, the CV curves tend to overlap, demonstrating that these two electrodes exhibit a gradually enhanced cycling stability for the insertion and extraction of lithium ions.[48,54]

The discharge/charge curves of pure anatase TiO_2 and TiO_2/$MnTiO_3$@C samples at a current density of 100 mA g^{-1} are shown in Fig. 8. The results of pure anatase TiO_2 (Fig. 8a) are generally consistent with the above CV analysis, in which two distinct potential plateaus appear at *ca.* 1.75 and 2.0 V for the discharging and charging processes, corresponding to Li^+ insertion/extraction within the TiO_2 lattice, respectively.[11,55] When the first cycle is completed, the cell exhibits initial discharge and charge capacities of 319.2 and 130.6 mA h g^{-1}, respectively, corresponding to the initial coulombic efficiency (the ratio of charge capacity to discharge capacity) of only 40.9%. The large capacity loss can be attributed to some lithium insertion into irreversible sites and the poor intrinsic electronic conductivity of TiO_2.[11] For the TiO_2/$MnTiO_3$@C sample (Fig. 8b), the voltage potential plateaus at 1.75 and 2.0 V are obviously shortened in contrast to the counterpart of TiO_2 in the initial three cathodic/anodic processes. Moreover, along with the cycles onward, the discharge and charge potential plateaus have gradually shortened to inconspicuous slopes after the

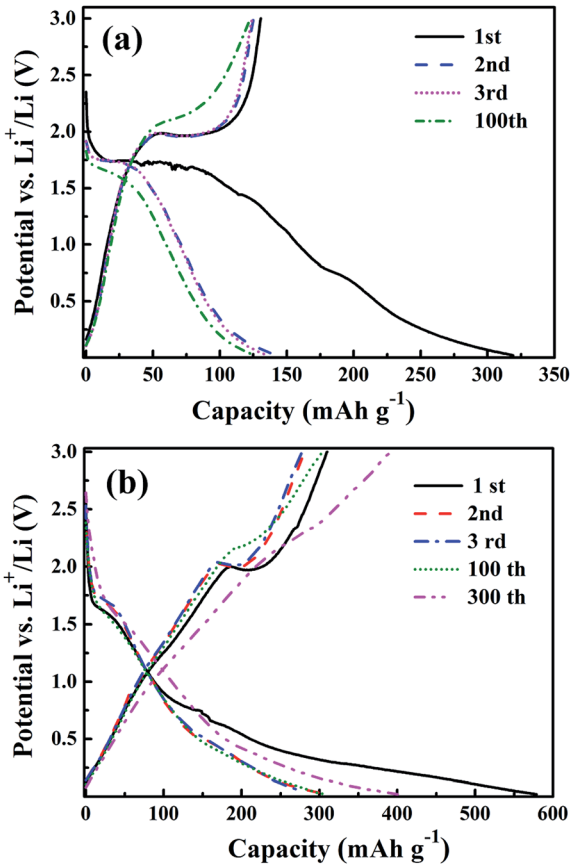

Fig. 8 Galvanostatic discharge/charge curves of the 1st, 2nd, 3rd, 100th and 300th cycles for porous pure TiO_2 and (b) $TiO_2/MnTiO_3$@C microspheres.

100th cycle, which may be attributed to the heterogeneous reaction mechanism between Li and the electrode materials including TiO_2 and $MnTiO_3$,[56] consistent with the CV measurement. With decreasing the voltage to 0.02 V in the first discharge process, the cell exhibits an initial specific capacity of 578.8 mA h g^{-1}, which is distinctly higher than the theoretical values of anatase TiO_2 (*ca.* 168 mA h g^{-1} for $Li_{0.5}TiO_2$), $MnTiO_3$ (*ca.* 533 mA h g^{-1}) and graphite (372 mA h g^{-1}). The reason can be attributed to the decomposition of the electrolyte and the formation of solid electrolyte interface (SEI) films.[57] Similar phenomena have also been found in other anode materials.[38,42] When the first charge was completed, a specific capacity of 310 mA h g^{-1} was obtained, and the initial coulombic efficiency was 53.6%, obviously higher than that (40.9%) of TiO_2. After 300 cycles, the retained capacity was 402.6 mA h g^{-1}, higher than the initial one (310 mA h g^{-1}), attributed to a gradual activation process of the electrode made of transition-metal oxides.[17]

From the cycling performance at a current density of 100 mA g^{-1} (Fig. 9a), the reversible capacity of $TiO_2/MnTiO_3$@C is found to be 402.6 mA h g^{-1} after 300 cycles and the retained capacity increases gradually along with the cycles onward. Meanwhile, the coulombic efficiency quickly reaches 90% in the second cycle, even remains more than 98% from the third to the 300th cycle. To reveal the prominent cycling performance of $TiO_2/MnTiO_3$@C, the LIBs consisting of pure anatase TiO_2, TiO_2/Mn_3O_4, TiO_2@C porous microspheres, and $MnTiO_3$@C nanoparticles were also investigated. Fig. 9b shows the charge/discharge capacities *versus* cycle number at a current density of 100 mA g^{-1} up to 100 cycles. The first charge/discharge capacities of these samples are 120.6/319.2 mA h g^{-1} (for TiO_2), 230.5/524.7 mA h g^{-1} (for TiO_2/Mn_3O_4), 299.6/541 mA h g^{-1} (for TiO_2@C), and 207.5/573.8 mA h g^{-1} (for $MnTiO_3$@C), respectively, which are lower than those of $TiO_2/MnTiO_3$@C (310/578.8 mA h g^{-1}). In addition, all these samples exhibited lower capacities in the successive cycles up to the 100th cycle, compared with $TiO_2/MnTiO_3$@C. The superior cycling performance of $TiO_2/MnTiO_3$@C is mainly attributed to the synergistic effect caused by the stable structure of TiO_2, the high capacity of $MnTiO_3$ and the excellent electrical conductivity of the carbon coating. The cyclic stability of the $TiO_2/MnTiO_3$@C electrode was further investigated at different current rates. From the rate capability shown in Fig. 9c, it is observed that the $TiO_2/MnTiO_3$@C electrode achieves reversible capacities of 259.8, 237.3, 200.4, 150.5, and 103.3 mA h g^{-1} at the current densities of 100, 200, 400, 800 and 1600 mA g^{-1}, respectively, which are obviously higher than those of pure anatase TiO_2 and $MnTiO_3$@C and close to those of TiO_2@C at the corresponding densities. The detailed data are listed in Table S1 (shown in the ESI†). It is noted that, when the current density was recovered to 100 mA g^{-1} after the rate performance test, the reversible capacities of all these samples returned back to their initial value approximately except for the $TiO_2/MnTiO_3$@C electrode, which reached *ca.* 330.2 mA h g^{-1}, higher than the value (259.8 mA h g^{-1}) acquired at the initial density of 100 mA g^{-1}, suggesting that the high current charge/discharge process not only did little to break down the integrity of the electrode, but also led to a gradual activation of the electrode material, which has also been found in other anode nanomaterials.[17,23,43] On the basis of the above results, the $TiO_2/MnTiO_3$@C electrode exhibits high reversible capacity, excellent cycling stability and long circling life than other samples, confirming that the ternary hybridization of TiO_2, $MnTiO_3$ and carbon is an efficient way to achieve the enhancement of electrochemical performance of TiO_2-based anode materials. Simultaneously, compared with recent research studies on the TiO_2-based composite anodes for LIBs summarized in Table S2 (shown in the ESI†), the as-prepared $TiO_2/MnTiO_3$@C anode also exhibits higher capacity retention and longer cycling performance even at large current density, further indicating that the $TiO_2/MnTiO_3$@C electrode is a promising candidate for LIBs with long lifespan and high power density.

To further investigate the electrochemical performances of $TiO_2/MnTiO_3$@C porous microspheres, electrochemical impedance spectroscopy (EIS) measurements were conducted on the cells after 100 cycles at a current density of 100 mA g^{-1}, Fig. 10. The Nyquist plot of each cell is comprised of an arc in the high- and medium-frequency region, and an inclined line in the low frequency region.[58] The diameter of the semicircle is directly proportional to the impedance, which contains electrolyte resistance (R_e), surface film resistance (R_{sf}) and charge transfer resistance (R_{ct}).[59–61] The inclined line is related to the

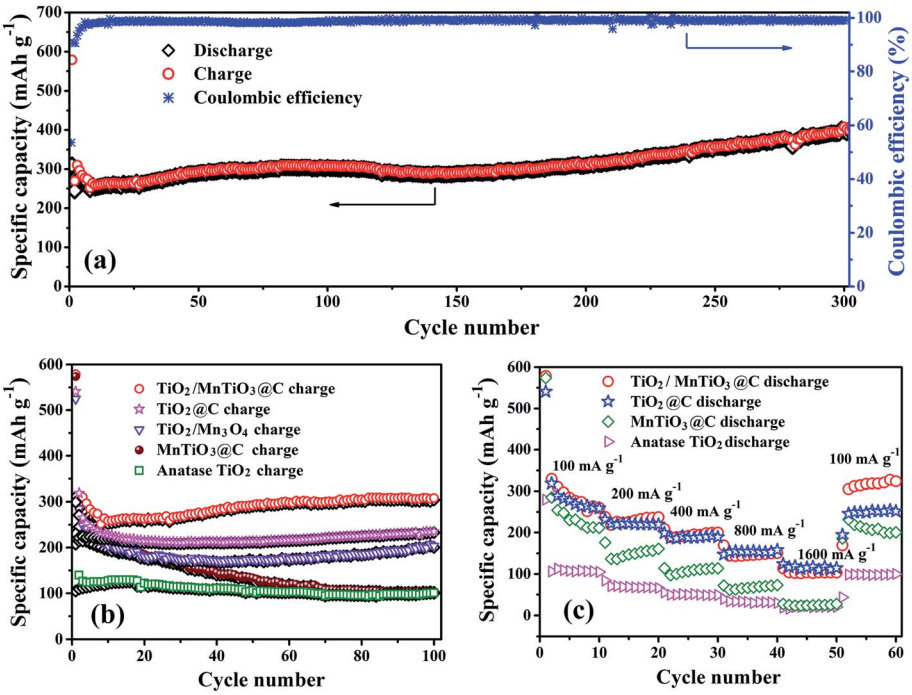

Fig. 9 Long-term cycling performance and coulombic efficiency of TiO_2/$MnTiO_3$@C at a current density of 100 mA h g^{-1} (a), cycling performance of TiO_2, TiO_2@C, $MnTiO_3$@C, TiO_2/Mn_3O_4 and TiO_2/$MnTiO_3$@C at a current density of 100 mA h g^{-1} (b), and rate capabilities of TiO_2, TiO_2@C, $MnTiO_3$@C and TiO_2/$MnTiO_3$@C (c).

lithium-ion diffusion inside the electrode materials corresponding to the Warburg impedance (Z_w).[62,63] The impedance spectra can be fitted based on a reasonable equivalent circuit (inset of Fig. 10), in accordance with the Li-ion insertion/extraction mechanism in the electrode.[59] The fitted curves are in accordance with the experimental data and the CPE in this model expresses a double layer capacitance (inset of Fig. 10). It is found that the ($R_e + R_{sf} + R_{ct}$) value of TiO_2/$MnTiO_3$@C (*ca.* 150 Ω) is much lower than that of the pure TiO_2 sample (*ca.* 350 Ω), indicating that the addition of carbon and $MnTiO_3$ largely improves the electrochemical activity of the TiO_2. Meanwhile, the TiO_2/$MnTiO_3$@C electrodes exhibit a larger slope at low frequency than pure TiO_2, suggesting that the lithium ion diffusion in electrodes has also been improved. The main reason could be attributed to the formation of a more loose structure (Fig. 3c) and the increased pore volume (Fig. 5) of TiO_2/$MnTiO_3$@C after the Mn_3O_4 doping and carbonization, which are beneficial to lithium ion diffusion. Therefore, the addition of carbon and $MnTiO_3$ in the composites can not only provide good electrode electron contact and electrical conductivity, but also facilitate lithium ion diffusion, favorable for the capacity enhancement of TiO_2/$MnTiO_3$@C.

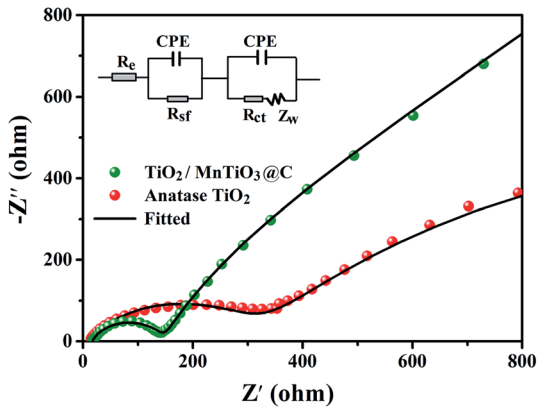

Fig. 10 The experimental and fitted Nyquist plots of pure TiO_2 and TiO_2/$MnTiO_3$@C. The inset is the corresponding equivalent circuit.

For the LIB anode material made from TiO_2/$MnTiO_3$@C composite microspheres, TiO_2 with little volume variation (less than 4%) serves as a matrix to relieve the stress and retains the structural stability of the anode material during the charge/discharge processes. In the TiO_2/Mn_3O_4 intermediate, Mn_3O_4 was transformed into $MnTiO_3$ completely by the reaction with carbon and TiO_2 after the carbonization process at 550 °C for 5 h (Fig. 1). The $MnTiO_3$ nanoparticles attached on the TiO_2 surface (Fig. 3d) enhanced the capacity of the LIB anode due to the higher theoretical capacity (533 mA h g^{-1}) than that (168 mA h g^{-1}) of anatase TiO_2. The presence of the carbon coating increases the electrical contact between $MnTiO_3$ and TiO_2 nanoparticles, avoiding effectively the electrical isolation of the TiO_2/$MnTiO_3$@C anode. As expected, the TiO_2/$MnTiO_3$@C porous composites exhibit higher cycling and rate performances than the corresponding TiO_2 porous microspheres.

4. Conclusions

In summary, TiO_2/$MnTiO_3$@C ternary hybrid porous microspheres have been synthesized by a facile approach. As anode

materials for Li-ion batteries, the porous composites exhibited superior cycling and rate performances by utilizing the structure stability of the TiO_2 matrix, high capacity of $MnTiO_3$ and superior electrical conductivity of the carbon coating during the charge/discharge processes. The attached $MnTiO_3$ on the TiO_2 matrix plays a significant role in improving the specific capacity of the TiO_2/$MnTiO_3$@C anode. Therefore, the research on the hybrid composites of TiO_2, $MnTiO_3$, and carbon coating demonstrates an efficient way to realize the enhancement of electrochemical performance of LIB anode materials.

Acknowledgements

This work was supported by the Fundamental Research Funds of Shandong University (2015JC016). The authors also acknowledge the financial support from the Doctoral Program of Higher Education of China (20130131110068), and Natural Science Fund for Distinguished Young Scholars of Shandong (JQ201312). Z. Guo appreciates the start-up fund from University of Tennessee Knoxville.

Notes and references

1 M. Wagemaker, A. Kentgens and F. M. Mulder, *Nature*, 2002, **418**, 397.
2 Y. S. Hu, L. Kienle, Y. G. Guo and J. Maier, *Adv. Mater.*, 2006, **18**, 1421.
3 H. Guo, W. Wang, L. Liu, Y. He, C. Li and Y. Wang, *Green Chem.*, 2013, **15**, 2810.
4 M. Leng, Y. Chen and J. Xue, *Nanoscale*, 2014, **6**, 8531.
5 D. Deng, M. G. Kim, J. Y. Lee and J. Cho, *Energy Environ. Sci.*, 2009, **2**, 818.
6 Y. Zhang, F. Du, X. Yan, Y. Jin, K. Zhu, X. Wang, H. Li, G. Chen, C. Wang and Y. Wei, *ACS Appl. Mater. Interfaces*, 2014, **6**, 4458.
7 G. Zhang, H. Duan, B. Lu and Z. Xu, *Nanoscale*, 2013, **5**, 5801.
8 F. Wu, X. Li, Z. Wang and H. Guo, *Nanoscale*, 2013, **5**, 6936.
9 L. Seon-Hong, Y. Ho-Gon, H. Kyu-Suk, J. Kim, J. In-Ho and S. Joo-Han, *J. Power Sources*, 2014, **247**, 307.
10 X. Li, Y. Zhang, T. Li, Q. Zhong, H. Li and J. Huang, *J. Power Sources*, 2014, **268**, 372.
11 X. Wang, Y. Wang, L. Yang, K. Wang, X. Lou and B. Cai, *J. Power Sources*, 2014, **262**, 72.
12 H. Wang, D. Ma, X. Huang, Y. Huang and X. Zhang, *Sci. Rep.*, 2012, **2**, 701.
13 V. Etacheri, Y. Kuo, A. van der Ven and B. M. Bartlett, *J. Mater. Chem. A*, 2013, **1**, 12028.
14 Z. Wen, S. Ci, S. Mao, S. Cui, Z. He and J. Chen, *Nanoscale Res. Lett.*, 2013, **8**, 499.
15 Y. Ma, G. Ji, B. Ding and J. Y. Lee, *J. Mater. Chem.*, 2012, **22**, 24380.
16 R. Mo, Z. Lei, K. Sun and D. Rooney, *Adv. Mater.*, 2014, **26**, 2084.
17 W. Luo, X. Hu, Y. Sun and Y. Huang, *J. Mater. Chem.*, 2012, **22**, 4910.
18 B. Li, Q. Zhang, C. Zhang, S. Kang, X. Li and Y. Wang, *Int. J. Electrochem. Sci.*, 2013, **8**, 8414.
19 P. Kubiak, M. Pfanzelt, J. Geserick, U. Hörmann, N. Hüsing, U. Kaiser and M. Wohlfahrt-Mehrens, *J. Power Sources*, 2009, **194**, 1099.
20 Q. Wang, Z. H. Wen and J. H. Li, *Adv. Funct. Mater.*, 2006, **16**, 2141.
21 J. Xu, C. Jia, B. Cao and W. F. Zhang, *Electrochim. Acta*, 2007, **52**, 8044.
22 L. Ren, Y. Liu, X. Qi, K. S. Hui, K. N. Hui, Z. Huang, J. Li, K. Huang and J. Zhong, *J. Mater. Chem.*, 2012, **22**, 21513.
23 J. Luo, X. Xia, Y. Luo, C. Guan, J. Liu, X. Qi, C. F. Ng, T. Yu, H. Zhang and H. J. Fan, *Adv. Energy Mater.*, 2013, **3**, 737.
24 J. Shin, D. Samuelis and J. Maier, *Adv. Funct. Mater.*, 2011, **21**, 3464.
25 P. S. Kumar, V. Aravindan, J. Sundaramurthy, V. Thavasi, S. G. Mhaisalkar, S. Ramakrishna and S. Madhavi, *RSC Adv.*, 2012, **2**, 7983.
26 I. Moriguchi, R. Hidaka, H. Yamada, T. Kudo, H. Murakami and N. Nakashima, *Adv. Mater.*, 2006, **18**, 69.
27 S. Yang, X. Feng and K. Müllen, *Adv. Mater.*, 2011, **23**, 3575.
28 P. Chang, C. Huang and R. Doong, *Carbon*, 2012, **50**, 4259.
29 S. H. Nam, H. Shim, Y. Kim, M. A. Dar, J. G. Kim and W. B. Kim, *ACS Appl. Mater. Interfaces*, 2010, **2**, 2046.
30 B. He, B. Dong and H. Li, *Electrochem. Commun.*, 2007, **9**, 425.
31 Y. Guo, Y. Hu, W. Sigle and J. Maier, *Adv. Mater.*, 2007, **19**, 2087.
32 B. Erjavec, R. Dominko, P. Umek, S. Sturm, S. Pejovnik, M. Gaberscek and J. Jamnik, *Electrochem. Commun.*, 2008, **10**, 926.
33 Y. Wang, T. Chen and Q. Mu, *J. Mater. Chem.*, 2011, **21**, 6006.
34 L. Tan, L. Pan, C. Cao, B. Wang and L. Li, *J. Power Sources*, 2014, **253**, 193.
35 Y. Wang, B. M. Smarsly and I. Djerdj, *Chem. Mater.*, 2010, **22**, 6624.
36 J. Jeong, D. Jung, E. W. Shin and E. Oh, *J. Alloys Compd.*, 2014, **604**, 226.
37 Z. Ali, S. N. Cha, J. I. Sohn, I. Shakir, C. Yan, J. M. Kim and D. J. Kang, *J. Mater. Chem.*, 2012, **22**, 17625.
38 X. Li, Y. Chen, H. Yao, X. Zhou, J. Yang, H. Huang, Y. Mai and L. Zhou, *RSC Adv.*, 2014, **4**, 39906.
39 Y. Tang, D. Wu, S. Chen, F. Zhang, J. Jia and X. Feng, *Energy Environ. Sci.*, 2013, **6**, 2447.
40 Z. Yang, Q. Meng, Z. Guo, X. Yu, T. Guo and R. Zeng, *J. Mater. Chem. A*, 2013, **1**, 10395.
41 T. Tao, A. M. Glushenkov, M. M. Rahman and Y. Chen, *Electrochim. Acta*, 2013, **108**, 127.
42 X. Guan, J. Zheng, M. Zhao, L. Li and G. Li, *RSC Adv.*, 2013, **3**, 13635.
43 J. Jiang, J. Luo, J. Zhu, X. Huang, J. Liu and T. Yu, *Nanoscale*, 2013, **5**, 8105.
44 H. B. Wu, X. W. D. Lou and H. H. Hng, *Chem.–Eur. J.*, 2012, **18**, 2094.
45 J. S. Chen, H. Liu, S. Z. Qiao and X. W. D. Lou, *J. Mater. Chem.*, 2011, **21**, 5687.
46 M. Zaki, *Thermochim. Acta*, 1997, **303**, 171.
47 S. Guo, G. Lu, S. Qiu, J. Liu, X. Wang, C. He, H. Wei, X. Yan and Z. Guo, *Nano Energy*, 2014, **9**, 41.

48 Y. Xia, Z. Xiao, X. Dou, H. Huang, X. Lu, R. Yan, Y. Gan, W. Zhu, J. Tu, W. Zhang and X. Tao, *ACS Nano*, 2013, **7**, 7083.
49 X. Su, Q. Wu, X. Zhan, J. Wu, S. Wei and Z. Guo, *J. Mater. Sci.*, 2012, **47**, 2519.
50 K. Zhang, P. Han, L. Gu, L. Zhang, Z. Liu, Q. Kong, C. Zhang, S. Dong, Z. Zhang, J. Yao, H. Xu, G. Cui and L. Chen, *ACS Appl. Mater. Interfaces*, 2012, **4**, 658.
51 W. Luo, X. Hu, Y. Sun and Y. Huang, *ACS Appl. Mater. Interfaces*, 2013, **5**, 1997.
52 C. Zhang, L. Fu, N. Liu, M. Liu, Y. Wang and Z. Liu, *Adv. Mater.*, 2011, **23**, 1020.
53 H. Gu, S. B. Rapole, J. Sharma, Y. Huang, D. Cao, H. A. Colorado, Z. Luo, N. Haldolaarachchige, D. P. Young, B. Walters, S. Wei and Z. Guo, *RSC Adv.*, 2012, **2**, 11007.
54 Z. Bai, N. Fan, Z. Ju, C. Guo, Y. Qian, B. Tang and S. Xiong, *J. Mater. Chem. A*, 2013, **1**, 10985.
55 S. Ding, J. S. Chen, Z. Wang, Y. L. Cheah, S. Madhavi, X. Hu and X. W. Lou, *J. Mater. Chem.*, 2011, **21**, 1677.
56 G. Huang, L. Zhang, F. Zhang and L. Wang, *Nanoscale*, 2014, **6**, 5509.
57 L. Hu, Y. Sun, F. Zhang and Q. Chen, *J. Alloys Compd.*, 2013, **576**, 86.
58 Q. Zhang, Z. Shi, Y. Deng, J. Zheng, G. Liu and G. Chen, *J. Power Sources*, 2012, **197**, 305.
59 W. Yue, S. Tao, J. Fu, Z. Gao and Y. Ren, *Carbon*, 2013, **65**, 97.
60 G. Lu, S. Qiu, H. Lv, Y. Fu, J. Liu, X. Li and Y. Bai, *Electrochim. Acta*, 2014, **146**, 249.
61 M. V. Reddy, T. Yu, C. H. Sow, Z. X. Shen, C. T. Lim, G. V. Subba Rao and B. V. R. Chowdari, *Adv. Funct. Mater.*, 2007, **17**, 2792.
62 J. Sun, K. Tang, X. Yu, J. Hu, H. Li and X. Huang, *Solid State Ionics*, 2008, **179**, 2390.
63 Y. Luo, D. Kong, J. Luo, S. Chen, D. Zhang, K. Qiu, X. Qi, H. Zhang, C. M. Li and T. Yu, *RSC Adv.*, 2013, **3**, 14413.

